Title:

Non-FG-Nups, ELYS and Nup35, coordinate an ordered assembly of FG-Nups on the scaffold of the nuclear pore complex

Author affiliation:

Hide A. Konishi[§] and Shige H. Yoshimura[*]

Laboratory of Plasma Membrane and Nuclear Signaling, Graduate School of Biostudies, Kyoto University, Yoshida Konoe, Sakyo-ku, Kyoto 606-8501, Japan

***Corresponding author:**

Shige H. Yoshimura

Laboratory of Plasma Membrane and Nuclear Signaling,

Graduate School of Biostudies, Kyoto University,

Yoshida Konoe, Sakyo-ku, Kyoto 606-8501, Japan

Tel & Fax: +81-75-753-7906

E-mail: yoshimura@lif.kyoto-u.ac.jp

[§]Current address: Laboratory of Chromosome and Cell Biology, The Rockefeller University, New York, NY 10065, USA

Summary

In this study, we examined how channel-forming subunits of the nuclear pore complex (NPC) are assembled into a selective channel within a highly structured scaffold ring during post-mitotic assembly. We focused on non-structured domains of the scaffold Nups and performed *in vitro* self-assembled particle assays with those derived from channel-forming FG-Nups. We found that non-structured domains of ELYS and Nup35N interacted with channel-forming FG-Nups to form a self-assembled particle. Sequential addition of FG-Nups into the scaffold particle revealed that ELYS, which initiates post-mitotic NPC reassembly, interacts with early assembling FG-Nups (Nups98 and 153) but not middle stage–assembling FG-Nups (Nups58 and 62). Nup35, which assembles between the early and middle stages, facilitated the assembly of Nup62 into the early assembling Nups both *in vitro* and *in vivo*. These results demonstrate that ELYS and Nup35 play a critical role in the ordered assembly of channel-forming FG-Nups during mitosis.

Keywords

Nuclear pore complex, Phase separation, Intrinsically disordered region, Molecular crowding, Self-assembly

Introduction

One of the largest protein complexes in eukaryotic cells is the nuclear pore complex (NPC), which spans the nuclear membrane and functions as the sole gate for macromolecular trafficking between the cytoplasm and nucleoplasm (Maximiliano A. D'Angelo and Martin W. Hetzer, 2008). The NPC is composed of several copies of more than 30 different nucleoporin (Nup) subunits (Elad et al., 2009). The NPC comprises several structurally distinct domains, such as the nuclear basket, cytoplasmic fibril, scaffold, and central channel, each of which is composed of defined sets of Nups. A number of studies using crystallography and electron tomography have revealed the molecular structures of the Nups and sub-complexes that comprise the scaffold (von Appen et al., 2015). The entire architecture of the scaffold was then composited by integrating all available structural information for each of the subunits and sub-complexes with information regarding protein-protein interactions (Fischer et al., 2015). Despite the low degree of amino acid conservation between Nups among different species, the entire architecture of the scaffold turned out to be well conserved. The outer ring containing the Nup107-160 sub-complex (Y-complex) is located at both the cytoplasmic and nucleoplasmic rims, and the inner ring, which contains the Nup93 sub-complex, is located deeper in the pore and connects the membrane and the central channel (von Appen et al., 2015; Fischer et al., 2015). Interactions between structured Nups and sub-complexes is thought to be stereospecific, resulting in a rigid architecture in the nuclear envelope.

In contrast to the scaffold, the central channel is formed primarily by a number of non-structured domains of Nups, which assemble via promiscuous interactions to form a highly crowded environment within the pore (Konishi et al., 2017). Nups containing a large number of phenylalanine-glycine (FG) motifs (FG-Nups) in a long intrinsically disordered region (IDR-Nups) (Denning et al., 2003; Rabut et al., 2004) form a molecular sieve-like environment that functions as a

selective barrier with respect to molecular transport. Small molecules (<40 kDa) diffuse passively, but large molecules (>40 kDa) are repelled unless they are carried by an appropriate transport receptor, such as a karyopherin (Elad et al., 2009; Mohr et al., 2009). Although several experimental and/or schematic models have been proposed to explain the structure and function of the barrier (Frey and Görlich, 2007; Patel et al., 2007), the molecular mechanism through which a large number of promiscuous interactions among IDR-Nups constructs a functional barrier within the rigid scaffold remains poorly understood.

Several lines of evidence have provided clues to enhance understanding of the mechanism of channel formation. Several FG-Nups self-assemble and form a hydrogel (Frey and Görlich, 2007; Frey et al., 2006) via hydrophobic interactions between Phe residues at a high protein concentration (≈10 mM) (Schmidt and Görlich, 2015). A recent study reported that FG-domains of Nup98 spontaneously self-assemble into phase-separated particles *in vitro* at physiologic concentrations (≈10 μM) (Schmidt and Görlich, 2015). These findings suggest that the central channel of the NPC forms via self-assembly of non-structured FG-Nups. Another study using a crowding-sensitive fluorescent probe demonstrated that protein crowding is not homogeneous throughout the channel; “protein-rich” domains lie at both rims of the channel but not in the central cavity (Konishi et al., 2017). This *in vivo* evidence suggests that even though FG-Nups self-assemble into protein-rich phases, several sets of Nups preferentially assemble into distinct protein-rich phases, possibly one at the cytoplasmic rim and another at the nucleoplasmic rim of the central channel. Furthermore, live-cell imaging of individual Nups during post-mitotic assembly of the NPC demonstrated that individual FG-Nups assemble on the chromosome surface in a defined order (Dultz et al., 2008; Konishi et al., 2017; Otsuka et al., 2014), suggesting that the assembly of FG-Nups is driven by a specific molecular mechanism and does not proceed solely via a random self-assembly–driven

mechanism. Collectively, this evidence suggests that although FG-Nups self-assemble into protein-rich phases, a specific molecular mechanism regulates and/or coordinates the assembly of FG-Nups to construct distinct protein-rich phases within the central channel.

In this study, we focused on IDRs from FG-Nups in the central channel, as well as those from non–FG-Nups in the scaffold, and examined how they assemble and interact using an *in vitro* self-assembled particle assay. The results demonstrated that some non–FG-Nups, Nup35 and ELYS, interact with distinct sets of FG-Nups in a self-assembled particle and facilitate interactions with another set of FG-Nups. Our data suggest that IDRs in non–FG-Nups play an important role in the ordered assembly of FG-Nups to construct the functional selective barrier in the central channel of the NPC.

Results

Both FG-rich and non-FG IDRs form self-assembled particles in a crowded environment

Almost all FG-Nups contain a long stretch of IDRs (Figure S1A), each of which normally contains a number of FG motifs. In contrast, most non–FG-Nups do not carry IDRs, with the exception of Nup35, ELYS, and Tpr (Figure S1A). Nup35, which is found in the inner ring complex, contains a long IDR at its N-terminus (a.a. 1-160). ELYS, a component of the Y-complex in the outer ring, contains IDRs in the C-terminal half of the molecule (a.a. 1310-1559 and 1851-2275). Tpr is a component of the nuclear basket and has an extremely high number of IDRs throughout the molecule (especially in the C-terminal half). We focused on examining the interactions of these IDRs from non–FG-Nups, together with a number of FG-rich IDRs from FG-Nups (Nups214, 153, 98, 62, 58, and 50). IDR fragments examined in this study are summarized in Figure 1A and Table S1. Most IDRs from FG-Nups contain a large number of FG motifs, whereas Nup214-C and Nup50FG have only a few FG motifs and a relatively high content of charged residues (Figure 1). The IDRs from non–FG-Nups have almost no FG motifs and are extremely rich in charged residues (Figure 1A). Purified IDR fragments were labeled with fluorescent dye, diluted into varying concentrations of polyethylene glycol (PEG)-containing buffer, and then observed under a fluorescence microscope. As summarized in Figure 1B-I, some of the IDR fragments formed self-assembled particles in a PEG-dependent manner. Among FG-rich IDRs, Nups214FG, 153FG, 98FG, and 62FG self-assembled (Figure S1B-E), whereas Nups214-C, 58FG-N, 58FG-C, and 50FG did not (Figure S1F-I). The ability of forming particles appeared to correlate well with the FG content (Figure 1A). A FG-rich IDR from Nup214 (Nup214FG, containing 28 FG motifs) formed particles at a low PEG concentration, whereas Nup214-C (4 FG motifs) and Nup50FG (2 FG motifs) did not form particles even at a high PEG concentration (Figures 1D, S1H and S1I), suggesting that hydrophobic

interactions are involved in particle formation by FG-rich IDRs (see later section, *Self-assembly of FG-rich IDRs and some non-FG IDRs is driven by hydrophobic interactions*).

Interestingly, some of the non-FG IDRs (Nup35N, ELYS-C1, -C2, and Tpr-IDR1) also formed self-assembled particles even though they do not contain FG motifs, but others did not (ELYS-M and Tpr-IDR2) (Figures 1F-I, S1J-M, -N, and -O). Amino acid sequence analyses revealed that all of these IDRs contained a number of charged residues, but only ELYS-M and Tpr-IDR2 had a large negative net charge (>20, Figure 1A and Table S1). This result suggests that particle formation by non-FG IDRs is driven predominantly by electrostatic interactions, but a large negative net charge may interfere with particle formation. Analysis of the secondary structure revealed that Tpr-IDR1, but not other IDRs, had a relatively high degree of coiled-coil structure (Figure S2B), although all of them had a high disorder probability. Circular dichroism (CD) spectra of Tpr-IDR1 indeed exhibited peaks at 222 nm and 207 nm, which indicates the presence of an α-helix (Figure S2C). These results suggest that coiled-coil interactions contribute to the formation of self-assembled particles by Tpr-IDR1, as demonstrated in a previous study (Woodruff et al., 2015).

FG-rich IDRs in self-assembled particle exhibited a very slow exchange rate with the extra-particle environment and low mobility within the particle, as determined by fluorescence recovery after photobleaching (FRAP) analysis (Figure S2D-F), consistent with a previous report regarding Nup98 (Schmidt and Görlich, 2015). In contrast, non-FG IDRs within particles exhibited faster recovery than FG-Nups (Figure S2G-I).

Self-assembly of FG-rich IDRs and some non-FG IDRs is driven by hydrophobic interactions

We next characterized the protein-protein interactions that induce self-assembly of IDR-Nups by employing two reagents to quantify hydrophobic and electrostatic interactions: 1,6-hexanediol, an

aliphatic alcohol that weakens hydrophobic interactions (Patel et al., 2007); and NaCl, which strengthens hydrophobic interactions but weakens electrostatic interactions. Self-organization of FG-rich IDRs (Nup98FG and Nup214FG) was significantly inhibited with increasing concentrations of 1,6-hexanediol (Figures 2A, B and S3A), strongly indicating the involvement of hydrophobic interactions in particle assembly. NaCl had less of an effect on FG-rich IDRs compared with 1,6-hexanediol; assembly of Nup214FG increased slightly (15-20%), whereas that of Nup98FG declined by 35-40% with increasing NaCl concentrations (Figures 2A, 2B, and S3B). To confirm the involvement of hydrophobic interactions in particle formation by FG-rich IDRs, particle formation was compared using FG-rich IDRs in which Phe residues were replaced with Ala residues. As shown in Figure S3C, substitution of Phe residues in the FG-motifs of Nup62FG with Ala residues abolished particle formation. These results demonstrate that hydrophobic interactions between Phe residues is the major driving force in the self-assembly of FG-Nups.

In a clear contrast, the self-assembly of non-FG-Nup (Tpr-IDR1) was increased by 1,6-hexanediol but reduced with increasing NaCl concentrations (Figures 2C, S3A, and S3B), demonstrating that electrostatic interactions govern particle assembly. Interestingly, Nup35N, which is also a non-FG IDR but with a small number of charged residues (Figure 1A) and high content of hydrophobic residues (hydrophobic index: −0.21, Table S1), behaved as an FG-rich IDR; the particle mass increased as the NaCl concentration increased and declined as the 1,6-hexanediol concentration increased (Figures 2D, S3A, and S3B). Furthermore, ELYS-C1, a non-FG IDR containing a number of charged residues (Figure 1A), exhibited both electrostatic and hydrophobic characteristics (Figures 2E, S3A, and S3B). The assembly of ELYS-C1 was suppressed both by NaCl and 1,6-hexanediol, which could have been due to its unique amino acid sequence, which is characterized by short stretches (~20 amino acids) of charged and hydrophobic residues alternating with each other

throughout the fragment (~200 amino acids) (Figure S3D). These results are summarized in Figure 2F. Most of the FG-rich IDRs self-assembled via hydrophobic interactions, but some non-FG IDRs (ELYS-C1 and Nup35N) also formed particles via hydrophobic interactions.

IDRs in ELYS and Nup35 interact with FG-IDRs

Two different IDRs, each labeled with a different fluorescent dye, were mixed in the same tube and observed under a fluorescence microscope to examine their interaction (Figure 3). One IDR was defined as the "host", and the partition coefficient (PC) of the other IDR (client) in the host particle was then quantified (see Experimental Procedures). As summarized in Figure 3A-C, IDRs from FG-Nups generally co-localized well with FG-rich IDRs, although the individual PC value varied widely depending on the number of Phe and charged residues. FG-rich IDRs with a high FG content and a low content of charged residues (Nups214FG, 62FG, 98FG, and 153FG) exhibited high PC values, whereas IDRs with a low FG content and a high content of charged residues (Nups214-C, 58FG-C, and 50FG) exhibited low PC values (Figure 3A and C). In some cases, the client phase-separated from the host in the same particle (Figure 3B), probably due to differences in hydrophobicity; highly hydrophobic IDRs preferred to remain in the less-hydrophobic client particle to avoid contact with the water phase.

The interactions between non-FG IDRs (ELYS-C1, Nup35N, and Tpr-IDR1) and between non-FG IDRs and FG-rich IDRs were also examined (Figure 3D-F). Tpr-IDR1, which self-assembled primarily via electrostatic interactions (Figure 2C), did not co-localize with most of the FG-rich IDRs, except for Nup50FG (Figure 3F). In contrast, Nup35N, a non–FG-Nup that self-assembled via hydrophobic interactions (Figure 2D), co-localized with most of the FG-rich IDRs (Nups153FG, 98FG, 58FG-N, 62FG, and 214FG) (Figure 3F). Similarly, ELYS-C1 co-localized

with FG-rich IDRs (Figure 3F). These results agree well with those shown in Figure 2D and E, showing that Nup35 and ELYS-C1, both of which are derived from non–FG-Nups, self-assembled via hydrophobic interactions, suggesting that Nup35 and ELYS-C1 play a role in the linkage between FG-Nups in the central channel and non–FG-Nups in the scaffold.

ELYS-IDR interacts with early assembling but not middle stage–assembling FG-Nups

In mitosis, the NPC disassembles during prophase and reassembles during anaphase via the ordered assembly of individual Nups. ELYS has been shown to play a critical role in the initial step of reconstruction by binding to the chromosome surface (Gillespie et al., 2007). Nups located on the nucleoplasmic side of the central channel (e.g., Nups153 and 98) and some of the scaffold Nups (e.g., Nups133 and 160) (early assembling Nups) follow ELYS. Nups in the inner ring complex (Nups35 and 155) and membrane-spanning Nups (Pom121 and Ndc1) then assemble, which is followed by Nups in the central cavity (Nups54, 58, and 62) (Dultz et al., 2008; Otsuka et al., 2014) (Figure 4A). To elucidate how the ordered assembly of channel-forming FG-Nups is regulated, we sequentially added client IDRs and examined how they are incorporated into the ELYS-C1 particle (Figure 4B, upper panel).

IDRs from early assembling FG-Nups (Nups98FG and 153FG) were rapidly incorporated into the ELYS-C1 particle after addition (Figures 4C and S4A), consistent with the results shown in Figure 3D and F. Interestingly, lower amounts of 58FG-N (which assembles during the middle stage) were incorporated into the ELYS particle, compared with the early assembling Nups (Figure 4C). Furthermore, Nup62FG (which assembles during the middle to late stages) was not incorporated into the ELYS particle (Figure 4C), despite generally co-localizing in the same particle when mixed (Figure 3D and F). These results demonstrate a clear correlation between the interaction between

ELYS particle and the order of the FG-Nups during post-mitotic reassembly; ELYS, which binds to the chromosome surface at the beginning of NPC reassembly, readily recruits Nups98 and 153 (early assembling Nups) but not Nups58 and 62 (middle stage–assembling Nups).

Nup35 facilitates the assembly of middle stage–assembling Nups

In addition to ELYS, Nup35N also interacted with FG-rich IDRs in our particle assay (Figure 3). As Nup35 appears on the chromosome surface during the early to middle stages of post-mitotic reassembly (Otsuka and Ellenberg, 2017) (Figure 4A) and interacts with the structured domain of Nup62 (Fischer et al., 2015), it can be hypothesized that it facilitates the assembly of middle stage–assembling FG-Nups. We therefore tested the capacity of Nup35N to facilitate the incorporation of middle stage–assembling Nups into ELYS particles. Nup35N was pre-incorporated into the ELYS-C1 particle in part to mimic the early to middle stages of post-mitotic reassembly (Figure 4B lower panel). As shown in Figure 4D, Nup35N was incorporated into the ELYS-C1 particle at a rate comparable to that of other early assembling Nups (Nups153FG and 98FG) (Figure 4C), consistent with results shown in Figure 3D and F. The middle stage–assembling Nup58 or 62 was then added, and its incorporated fluorescence signal in the particle was quantified. Interestingly, incorporation of Nup62FG into the ELYS-C1 particle was enhanced when the particle contained Nup35N (Figure 4E). A similar effect of Nup35N was observed with the incorporation of Nup58FG, although the effect was smaller (Figure 4F). It should be noted that no such stimulatory effect was observed with Nup98FG, an early assembling FG-Nup; pre-incorporation of Nup98FG into ELYS-C1 particle did not facilitate the incorporation of Nups62 and 58 (Figure 4E and F). These results demonstrate that Nup35N facilitates the interaction of middle stage–assembling Nups with early assembling Nups.

Finally, we examined the role of Nup35 in the post-mitotic NPC reassembly process *in vivo*. An EGFP-fused FG-Nup (Nup62 or 153) was expressed in Nup35 (or control) knock-down (KD) cells, and the appearance of fluorescence signals on the chromosome rim during telophase and anaphase was observed by time-lapse imaging. Signal associated with Nup62 began to appear on the chromosome surface 6-9 min after anaphase onset and increased until ~15 min in the control cells (Figure 4G). In contrast, Nup35-KD cells exhibited a significant delay in Nup62 assembly, which began to appear after 10 min and slowly increased until 40 min after anaphase onset. It should be noted that the effect of Nup35 KD was not observed in the assembly of Nup153, an early assembling Nup; it began to appear 3-5 min and saturated 10-12 min after anaphase onset in both control and Nup35-KD cells (Figure 4H). These results provide clear *in vivo* evidence that Nup35 facilitates the assembly of middle stage–assembling Nups during post-mitotic NPC reassembly.

Discussion

In this study, we investigated the self-assembling properties of IDRs derived from FG-Nups and non–FG-Nups as well as their interaction patterns using an *in vitro* particle formation assay. The results demonstrated that i) many FG-rich IDRs self-assemble via hydrophobic interactions and co-assemble (co-localize) well in the same particle; ii) some IDRs from non–FG-Nups self-assemble via electrostatic interactions, whereas others (Nup35N and ELYS-C1) assemble via hydrophobic interactions and interact with FG-rich IDRs; iii) The IDR of ELYS (ELYS-C1) interacts with early assembling FG-rich IDRs (Nups98FG and 153FG) but not with middle stage–assembling Nups (Nups58 and 62); and iv) Nup35N facilitates the assembly of middle stage–assembling FG-rich IDRs (Nups58FG and 62FG) into the ELYS particle. These results demonstrate the important roles of IDRs from scaffold Nups in coordinating the assembly of FG-Nups. It can be hypothesized that

although self-assembly of Nups is generally driven via promiscuous interactions among IDRs, "ordered" assembly of Nups and the construction of a functional selective channel during the post-mitotic reassembly process could be mediated by a few "facilitator subunits," such as ELYS and Nup35. Functional analyses of these mediator subunits could elucidate the mechanism underlying the construction of the central channel, and together with structural information regarding the scaffold, such analyses could elucidate the structure/function relationship of the entire NPC.

The molecular architecture of the scaffold has been studied extensively using crystallography, electron tomography, and mass spectroscopy (von Appen et al., 2015; Kim et al., 2018). Nup35 is a component of the Nup93 complex, which is the major structural unit of the inner ring, and interacts with Nups in the same complex (Nups93, 155, and 205) as well as other Nups (Nup98 and Ndc1) and the membrane (Fischer et al., 2015). A recent study reported the crystal structure of the Nup93 complex with structured domains of the central channel components Nups62, 58, and 54 (Chug et al., 2015), demonstrating that the Nup93 complex links the scaffold and central channel. Although the entire structure of Nup35 was not elucidated in the crystallographic study, it is possible that the IDR of Nup35 associates with the IDRs of Nups62, 54, and 58. Our *in vitro* particle assay indeed demonstrated that Nup35N, which has no FG motif, interacted with most of the FG-rich IDRs examined (Figure 3D and F).

From a structural perspective, the interaction between Nup35N and FG-rich IDRs could be attributed to its unique amino acid composition, which is rich in proline (≈20%) and glycine (≈11%) (Figure S3E). A large number of proline residues could aid the formation of self-assembling particles, as well as hydrophobic interactions with FG-rich IDRs. It was previously demonstrated that interactions between proline-rich motifs in N-WASP and the SH3 domain of a partner molecule are important for phase separation (Li et al., 2012). Proline is also known to break secondary structures

(α-helixes and β-sheets) (O'Neil and DeGrado, 1990; Piela et al., 1987; Rauscher et al., 2006) and confer a high degree of flexibility on polypeptides. Such flexibility could increase the mobility of molecules within the particle, thus facilitating the incorporation of other molecules into the host particle.

In addition to Nup35, a fragment of the ELYS IDR (ELYS-C1) also interacted with FG-rich IDRs, indicating that it functions as a facilitator between the scaffold and central channel. ELYS contains several distinct functional domains in addition to its IDR and was shown to play an important role in the initial step of post-mitotic NPC reassembly. ELYS binds to the chromosome surface via its AT-hook domain (aa. 1971-1983) (Gillespie et al., 2007), which recruits early assembling Nups such as the Nup107-160 complex and Nups98 and 153. The AT-hook domain is located within the ELYS-C1 fragment examined in this study. Therefore, it can be hypothesized that the C-terminal domain of ELYS functions as a platform for the successive assembly of FG-Nups via hydrophobic interactions. In contrast, the structured N-terminal domain interacts directly with a helical domain of Nup120 (human Nup160) in the Y-complex (Bilokapic and Schwartz, 2012). Therefore, it seems likely that the structured N-terminal domain of ELYS acts as a stereospecific binding site for the scaffold Y-complex, whereas the non-structured C-terminal region binds to the chromosome surface and initiates the ordered assembly of FG-Nups (Figure 4I).

Considering the mediator function of ELYS and Nup35 in conjunction with the self-assembling characteristics of FG-Nups, it seems likely that reconstruction of the functional NPC during mitosis is driven by both promiscuous interactions among IDRs and stereospecific interactions among scaffold Nups, which are linked by unique Nup IDRs such as ELYS and Nup35N (Figure 4I). ELYS initiates the reassembly process by binding to the chromosome surface via its AT-hook domain. ELYS then recruits both scaffold Nups (Nups in the Y-complex), primarily via

stereospecific interactions involving the N-terminus, and IDRs of early assembling FG-Nups (Nups153 and 98), primarily via promiscuous interactions involving the C-terminal IDR. The middle stage–assembling Nups58 and 62 cannot enter this IDR-rich phase at this stage. Nup35 eventually assembles into the IDR-rich phase formed at the ELYS C-terminus and then recruits the middle- to late-stage assembling Nups58 and 62. Simultaneously, the N-terminus of Nup35 appears to interact with the scaffold via the Nup93 complex (Fischer et al., 2015) to link the FG-rich IDR phase to the entire scaffold. In the later stages, cytoplasmic Nups (Nups214 and 358) in addition to other Nups (Tpr, etc.) associate, potentially inducing further rearrangements of the IDR phase to establish the functional selective barrier within the NPC. It could be intriguing to investigate how phosphorylation/dephosphorylation of Nups (such as the Nup107-160 complex (Glavy et al., 2007), Nup35 (Linder et al., 2017), and Nup98 (Laurell et al., 2011) is involved in the regulation of Nup reassembly.

Experimental procedure

Amino acid sequence analyses

The disordered propensity was analyzed by DisProt server (http://disorder.compbio.iupui.edu/metapredictor.php) with a PONDR-fit algorithm. The net charge and the charge distribution were analyzed by a protein calculator (INNOVAGEN, https://pepcalc.com/protein-calculator.php), and EMBOSS explorer (http://www.bioinformatics.nl/cgi-bin/emboss/charge?_pref_hide_optional=1), respectively. The hydrophobicity was analyzed by ProtScale server in ExPASy (https://web.expasy.org/protscale/) by using Kyte & Doolittle method. COILS server in ExPASy (https://embnet.vital-it.ch/software/COILS_form.html) was used for coiled-coil analysis.

DNA construction and protein purification

cDNA fragments encoding human Nup50FG (aa. 1–145), rat Nup62FG (aa. 1–268), human Nup98FG (aa. 214–480), human Nup153FG (aa. 1190–1464), human Nup214FG (aa. 1786–2090), human Nup214-C (aa. 1251–1550), human Nup35N (aa. 1–160), human Tpr-IDR1 (aa. 1451–1689), and human Tpr-IDR2 (aa. 1690–1937) were amplified by PCR from the full-length cDNA and sub-cloned into pET28-a (+) or pET28-b (+) (Novagen). Human Nup58FG-N (aa. 1–250), -C (aa. 438–599), human ELYS-IDR-M (aa. 1310-1559), human ELYS-IDR-C1 (aa. 1851-2033), and human ELYS-IDR-C2 (aa. 2034-2275) were artificially synthesized with the codon usage optimized for bacterial expression (Thermo Fisher Scientific), and sub-cloned into pET28-a (+). For IDRs lacking endogenous cysteine residue, a single cysteine was added to the carboxyl-terminal end of the fragment either by PCR or during artificial synthesis. Phe residues in Nup62 (aa. 4, 6, 16, 18, 44, 46, 75, 77, 140, and 142) were substituted by Ala by PCR.

The expression of His_6-tagged IDR-fragment in *Escherichia coli* cells (BL21-CodonPlus(DE3)-RIL, Agilent Technologies, Wilmington, DE) was induced by 0.5 mM IPTG at 37°C for 3 hours. The cells were harvested by centrifugation (5,000x g, 4°C, 15 min), and dissolved in Denaturing Buffer (8 M urea, 100 mM $NaPO_4$, 10 mM Tris-HCl, 5 mM 2-mercaptoethanol (2-Me) (Nacalai Tesque, Kyoto, Japan), 10 mM imidazole, pH 8.0) at 4°C for 16 hours with a gentle agitation. An insoluble fraction was separated by centrifugation (10,000x g, 4°C, 30 min), and the supernatant was then incubated with Ni-NTA agarose beads (QIAGEN) at 4°C for 2 hours or at room temperature for 30 min. The beads were washed for several times with Denaturing Buffer containing 20 or 25 mM imidazole. His-tagged protein was eluted by 200 or 300 mM imidazole in Denaturing Buffer.

Purified protein was dialyzed against 0.1% (v/v) trifluoroacetic acid (TFA) (Nacalai Tesque) with 2 mM 2-Me at 4°C for 3 hours, and subsequently against 0.1% (v/v) TFA with 2 mM 2-Me at 4°C for ~20 hours. It was finally dialyzed against 0.05% (v/v) TFA, without 2-Me at 4°C for 2-3 hours, lyophilized (FDU-2200, EYELA), and stored at 4°C until use. Purified protein for CD measurement (Nup58CC (aa. 256-381) and Nup58FG-N) was first dialyzed against a buffer containing 100 mM L-arginine (50 mM KPO_4, 100 mM L-arginine, 150 mM NaCl, 2 mM 2-Me), then against 50 mM L-arginine, and finally against 50 mM HEPES (pH 7.4) with 100 mM NaCl and 2 mM 2-Me at 4°C for 1 day, and stored -80°C by flash freezing with liquid nitrogen. The final protein concentration was determined by using Coomassie brilliant blue (CBB) staining, with bovine serum albumin (BSA) as a standard.

Protein labeling

purified IDR-Nups' fragments were labeled by utilizing maleimide reaction with artificially added cysteine in the carboxyl terminal of each IDR-fragment or endogenous cysteine for some Nups (Nups214 and Nup58FG-C). Using ATTO dyes (ATTO390, 488, and 610, ATTO-TEC) dissolved in anhydrous DMSO (Nacalai Tesque), the appropriate volume of the ATTO solution was added in the protein stock buffer (final, 10 mM) before dissolving the lyophilized proteins. To stop the maleimide reaction, final 5 mM of dithiothreitol (DTT, Nacalai Tesque) was added into the denaturing protein stock solution and incubated at 4℃ for more than 12 hours.

In vitro phase separation assay

Lyophilized proteins were dissolved in a small volume (~50 μL) of protein stock buffer (2 M Guanidine hydrochloride, 100 mM Tris-HCl, 10 mM HEPES, pH 8.0) and stored at 4℃ for 1 day.

This stock solution (≈1200 μM) was quickly diluted (>100 times) into the assay buffer (50 mM HEPES, 100 mM NaCl, pH 7.4) containing varying concentrations of crowding agents, salt, or 1,6-hexanediol (Nacalai Tesque), after removing aggregates by centrifugation (5 min at 10,000 x g). For sequential partitioning assay, a client protein was added into the assay buffer containing the host protein particle. The final protein concentration was ≈ 2 μM for the client proteins and ≈3 μM for the host protein.

Microscopic observation, image processing and analysis

Protein solution containing self-assembled particles was applied to a 96-well glass bottom plate (IWAKI, Shizuoka, Japan) or a custom-made flow chamber. Microscopic observation was performed using FV3000 confocal laser-scanning microscope (OLYMPUS, Tokyo, Japan) using 60 × NA1.42 objective lens (PLAPON60XO) with oil immersion. For the total particle mass analysis, 10 images were randomly taken in 2x zoom field of 60 × objective lens. The excitation wavelength against ATTO390, 488, and 610 was 405 nm, 488 nm, and 564 nm, respectively. Sampling speed was 8.0 μs per pixel.

For *in vivo* live cell imaging, EGFP-fused Nups62 or 153 was co-expressed with mPlum (Clontech)-fused histone H3 in HeLa cells cultured in DMEM (SIGMA) supplemented with 10% FBS (Hyclone). Before the microscopic observations, the culture medium was replaced with phenol red-free medium. The stage-top chamber (Tokai-hit, Shizuoka, Japan) was filled with moisture using distilled water and 5 % CO_2, and was maintained at 37°C. Images were captured every 1 min between metaphase and early G1 phase. Signal intensity at chromosome rim was measured as described below.

Microscopic images were exported as raw tiff 8-bit images (512x512 pixels) and analyzed with particle analyzer plugin in FIJI macro (https://fiji.sc/). When analyzing self-assembled particles, the sum of the RawIntDen (Raw Integrated Density) of each particle per image (total particle mass) was measured. For obtaining the partition coefficient (PC) of a client protein, a threshold for the particle size (>1 μm in Feret's diameter) was applied to eliminate non-self-assembled aggregations. The ratio of the mean intensity of the client protein in the particle ($[I]_{particle}$) over that of the bulk solution ($[I]_{bulk}$) was calculated after the background subtraction and shown as common logarithm values. For the sequential partitioning assay, the threshold for the particles' size was set between 5 and 15 μm in Feret's diameter to avoid both small and large particles.

For analyzing GFP signal in HeLa cells, the chromosome rim was detected in mPlum-H3 image by using a particle analyzer of FIJI, converted to a region of interest (ROI), and finally applied to the image of GFP channel. The GFP signal intensity in the ROI was quantified, divided by that in the interphase cytoplasm, and normalized by a value at 45 min. Obtained data were arranged in Excel (Microsoft) and R version 3.4.1.

FRAP analysis

The self-assembled particle was formed by ATTO488-labeled IDR-Nups as described above. A half or a center of the particle was bleached by a 488 nm laser at the maximum output for 4 sec. After bleaching, the time lapse observation was continued every 10 sec. Signal intensity of the bleached region was quantified manually using the FIJI and the obtained values were processed as mentioned above, and shown as a relative intensity to the signal intensity before bleaching.

CD spectra measurement

The CD spectra of purified IDR-Nups and a coiled-coil protein (Nup58CC) were measured using a CD spectrophotometer (J-805, JASCO, Tokyo, Japan) with a 0.1 cm quartz cuvette. Data were acquired every 0.1 nm between 200 and 260 nm. Samples were prepared in assay buffer (50 mM HEPES pH 7.4, 100 mM NaCl, 2 mM 2-Me). The final protein concentration of Nup58FG-N, Nup58CC, Tpr-IDR1, and Tpr-IDR2 were 0.2, 0.2, 0.3, and 0.3 mg/mL, respectively.

Nup35 knockdown

Small interference RNAs for Nup35 and control (luciferase) were purchased from Thermo (Silencer Select siRNA #29400 for Nup35 and Stealth^{TM} RNAi 12935-146 for Luciferase). It was introduced into HeLa cells by Lipofectamine RNAi MAX (Invitrogen) by following the manufacturer's protocol.

Statistical analysis

To analyze the statistics for all of obtained data in this study, Welch two sample *t* test was used for normally distributed data, and Wilcoxon Rank-Sum test was used for non-normally distributed data. A Shapiro-Wilk normality test was used to determine whether data were distributed normally. All of statistical tests were done by using R version 3.4.1.

Author Contributions

H.A.K. planned the project, designed the experiments, performed all experiments, and wrote the paper. S.H.Y. planned the project, designed the experiments, performed live cell imaging, and wrote the paper.

Acknowledgements

We thank Prof. T. Haraguchi (human Nup98), Prof. K. Ullman (rat Nup62 and human Nup153), Prof. J. Ellenberg (human Nup214) for providing cDNAs encoding nucleoporins. We also thank S. Dodo for technical support, especially recombinant protein preparation. This study was supported financially by the Funding Program for Next Generation World-leading Researchers (S.H.Y., No. LS076), and a Grant-in-Aid for Scientific Research (B) (S.H.Y., No. 21370054) from the Japan Society for the Promotion of Science (JSPS).

Figure legends

Figure 1 Self-assembly of IDR-Nups

(A) Amino acid compositions of IDR fragments used in this study. Vertical lines indicate the positions of positively charged (blue), negatively charged (red), and hydrophobic (gray) amino acids, and FG motifs (black). For visibility, other amino acid residues (polar and non-polar) are not shown here. Amino acid positions in the full-length protein are shown at both ends. The number of FG-motifs, positively and negatively charged residues, as well as the ability of self-assembly are shown on the right. More detailed information on the amino acids composition is shown in Table S1. (B-I) DIC and fluorescence images of the self-assembled particles of Nup98FG (B), Nup153FG (C), Nup214FG (D), Nup62FG (E), Tpr-IDR1 (F), Nup35N (G), ELYS-C1 (H), and ELYS-C2 (I) in the presence or absence of 15 % PEG. Scale bar: 10 μm.

Figure 2 Self-assembly of IDR-Nups is driven by hydrophobic and/or electrostatic interactions

(A-E) Co-line plot of NaCl- and 1,6-hexanediol-dependency in self-assembly of IDR-Nups (Nup98FG (A), Nup214FG (B), Tpr-IDR1 (C), Nup35N (D), ELYS-C1 (E)). Data are represented as

mean ± SEM from three independent experiments. Each value is shown as a relative value to the standard condition (50 mM HEPES pH 7.4, 100 mM NaCl) in the presence or absence of 15 % PEG. (*: $p<0.05$, **: $p<0.005$, ***: $p<0.0005$). P-values were obtained by appropriate statistical tests (see Experimental Procedures).

(F) A summary of self-assembling properties of IDR-Nups. Hydrophobic-based (gray) and electrostatic-based (red) self-assembled IDR-Nups are highlighted.

Figure 3 Interaction diagram of IDR-Nups in a self-assembled particle

Interaction between FG-Nups (A-C), and between FG-Nup and non-FG-Nup (D-F) were examined.

(A and D) Fluorescence images of the self-assembled particle. Fluorescence signals of the host protein (labeled with ATTO390, left), and the client protein (labeled with ATTO488, middle), as well as the merged image, (right) are shown. Scale bar: 2 μm.

(B and E) Examples of phase separation of the host and the client in the same particle. Experimental procedure was same as in A and D.

(C and F) Tile plot of partition coefficient (PC) of client proteins against host proteins. Data are presented as an averaged value of the PC. An asterisk (*) indicates the phase-separation as shown in (B and E).

All of PC values are shown in Table S2.

Figure 4 Nup35 facilitates the assembly of middle-assembling FG-Nups during the post-mitotic NPC reassembly

(A) The order of Nup reassembly in the post-mitotic NPC reassembly. Early-, middle-, and late-stage assembling Nups are plotted along the time after anaphase onset.

(B) Experimental schemes of the *in vitro* sequential addition assay. A fluorescently-labeled client protein was added to the host particle (ELYS-C1) solution and the fluorescence signal was observed under the microscope (upper panel). Alternatively, a fluorescently-labeled 1st client was first added to the host particle solution, and then the 2nd client, which was labeled with different fluorescent dye, was sequentially added (lower panel).

(C) A summary of sequential addition assay. DIC image of the particle and the fluorescence images of the client (Nups98FG, 153FG, 58FG-N, and 62FG) are shown (upper panels). The fluorescence intensity of the client in the host particle was quantified and plotted in the bottom panel. Data are represented as mean ± SEM from three independent experiments. Multi-color images of both the host and the clients are shown in Figure S4A.

(D) Fluorescence images of Nup35N, which had been incorporated into the host particle (ELYS-C1). The plot was shown as in (A).

(E and F) Fluorescence images of the 2nd client proteins in the sequential addition assay. As described in B (bottom panel), the 1st client (Nup35N or Nup98FG) was first added to the host particle (ELYS-C1), and then the 2nd client (Nup62FG (E), Nup58FG-N (F)) was added. Images were taken 300 sec after the addition of the 2nd client protein. The fluorescence intensity of the 2nd client protein was quantified and plotted as a relative value to the value without the 1st client (none). Data are represented as mean ± SEM from three independent experiments. Scale bar: 20 µm. The multi-color images of the host (ELYS-C1) and the 1st client (Nup35N are shown in Figure S4B. *: $p<0.05$, **: $p<0.005$, ***: $p<0.0005$, n.s.: no significance. P-values were obtained by appropriate statistical tests (see Experimental Procedures) Scale bar: 20 µm in (C-F).

(G and H) The effect of Nup35-knock-down on the post-mitotic assembly of Nup153 and Nup62. EGFP-fused Nup62 (G) or Nup153 (H) was expressed in Nup35-knocked-down HeLa cells,

together with mPlum-fused histone H3, and was subjected to the time-lapse imaging during mitosis. Fluorescence signal at the chromosome rim was quantified and normalized with the signal in the cytoplasm in interphase. The value was represented as a relative value to that at 45 min as a maximum. Data are shown as mean ± SEM. The number of the analyzed cells is also indicated. Scale bar: 10 μm.

(I) Schematic model of the post-mitotic NPC reassembly. See text for detail.

Table S1 Amino acid compositions and characteristics of IDR-Nups used in this study

Table S2 Partition coefficient of client protein against host protein in the assay shown in Figure 3. Data are summarized and represented as mean ± SD from more than two independent experiments. n indicates the number of analyzed particles. NA: not assigned.

Figure S1 Self-assembly of IDR-Nups

(A) Disorder probability of Nups used in this study. The results of PONDR-fit algorism prediction are shown against amino acid position.

(B-E and J-M) DIC and fluorescence images of self-assembled particles formed by IDRs from FG-Nups (B-E) and non-FG-Nups (J-M) in different concentrations of PEG (left). The total particle mass (see Experimental Procedures) was measured and summarized in the right panel. Data are presented as mean ± SEM, from three independent experiments. (*: $p<0.05$, **: $p<0.005$, ***: $p<0.0005$). P-values were obtained by appropriate statistical tests (see Experimental Procedures).

(F-I, N and O) DIC and fluorescence images obtained from non-self-assembling Nups in the presence of 15% PEG. Scale bar: 10 μm.

Figure S2 Characterization of the self-assembling IDR-Nups

(A) Disorder probability of Tpr-IDRs. The result of PONDR-fit algorism prediction is shown.

(B) Co-line plot of the coiled-coil propensity (red) and the helix propensity (blue) of Tpr-IDRs.

(C) CD spectra of Tpr-IDR1 and Tpr-IDR2, Nup58FG-N and Nup58 (aa. 25-381). It was previously reported that Nup58FG-N is disordered and Nup58CC forms a stable coiled-coil (Solmaz et al., 2011).

(D-I) FRAP analysis of self-assembled particles (Nup98FG (D), Nup153FG (E), Nup214FG (F), Tpr-IDR1 (G), Nup35N (H), ELYS-C1 (I)). Fluorescence images before and after (0, 60, and 300 sec) bleaching (left panels), and signal intensity plot over time after the bleaching (right panel) are shown. Two different bleaching patterns (half; blue, centre; red) were tested. Data are represented as mean ± SD from three independent experiments.

Figure S3 Investigation of the driving force of self-assembly

(A and B) Fluorescence images of self-assembled particles in different concentrations of 1,6-hexanediol (A) and NaCl (B).

(C) FG-mutants of Nup62FG. Amino acid sequences (aa. 1-268) of Nup62 (wild-type and mutants) are shown. FG and FxFG motifs were mutated to AG and AxAG, respectively, as indicated in red. Fluorescence images of self-assembled particles are shown in the right panels. Scale bar: 20 µm.

(D) Co-line plot of charge (red) and hydrophobicity (black) of ELYS-C1 against the amino acid position.

(E) Amino acid sequence of Nup35N fragment. Proline and glycine residue are labeled in green and red, respectively.

Figure S4 Sequential assembly of IDR-Nups into a self-assembled particle of ELYS-C1

(A) DIC and fluorescence images of the host (ELYS-C1, blue) and the client proteins (green). Images were taken 3 min after the addition of the client. Scale bar: 20 µm.

(B) DIC and fluorescence images of the host (ELYS-C1, blue) and the 1st client (Nup35N or Nup98FG, red). The incorporation of the 1st client into the host particle was confirmed before the addition of the 2nd client protein. Scale bar: 20 µm.

(C) RNAi of Nup35. Small interference RNA for human Nup35 or luciferase was introduced into HeLa cells. The cell lysate was subjected to immunoblot analysis using anti-Nup35 and anti-β-actin antibodies. The position of Nup35 (~35 kDa) is indicated by an arrow.

Declaration of Interests

The authors declare no competing financial interests.

References

von Appen, A., Kosinski, J., Sparks, L., Ori, A., DiGuilio, A.L., Vollmer, B., Mackmull, M.-T., Banterle, N., Parca, L., Kastritis, P., et al. (2015). In situ structural analysis of the human nuclear pore complex. Nature *526*, 140–143.

Bilokapic, S., and Schwartz, T.U. (2012). Molecular basis for Nup37 and ELY5/ELYS recruitment to the nuclear pore complex. Proc. Natl. Acad. Sci. *109*, 15241–15246.

Chug, H., Trakhanov, S., Hülsmann, B.B., Pleiner, T., and Görlich, D. (2015). Crystal structure of the metazoan Nup62•Nup58•Nup54 nucleoporin complex. Science *350*, 106–110.

Denning, D.P., Patel, S.S., Uversky, V., Fink, A.L., and Rexach, M. (2003). Disorder in the nuclear

pore complex: the FG repeat regions of nucleoporins are natively unfolded. Proc. Natl. Acad. Sci. U. S. A. *100*, 2450–2455.

Dultz, E., Zanin, E., Wurzenberger, C., Braun, M., Rabut, G., Sironi, L., and Ellenberg, J. (2008). Systematic kinetic analysis of mitotic dis- and reassembly of the nuclear pore in living cells. J. Cell Biol. *180*, 857–865.

Elad, N., Maimon, T., Frenkiel-Krispin, D., Lim, R.Y., and Medalia, O. (2009). Structural analysis of the nuclear pore complex by integrated approaches. Curr. Opin. Struct. Biol. *19*, 226–232.

Fischer, J., Teimer, R., Amlacher, S., Kunze, R., and Hurt, E. (2015). Linker Nups connect the nuclear pore complex inner ring with the outer ring and transport channel. Nat. Struct. Mol. Biol. *22*, 774–781.

Frey, S., and Görlich, D. (2007). A saturated FG-repeat hydrogel can reproduce the permeability properties of nuclear pore complexes. Cell *130*, 512–523.

Frey, S., Richter, R.P., and Görlich, D. (2006). FG-rich repeats of nuclear pore proteins form a three-dimensional meshwork with hydrogel-like properties. Science *314*, 815–817.

Gillespie, P.J., Khoudoli, G. a, Stewart, G., Swedlow, J.R., and Blow, J.J. (2007). ELYS/MEL-28 chromatin association coordinates nuclear pore complex assembly and replication licensing. Curr. Biol. *17*, 1657–1662.

Glavy, J.S., Krutchinsky, A.N., Cristea, I.M., Berke, I.C., Boehmer, T., Blobel, G., and Chait, B.T. (2007). Cell-cycle-dependent phosphorylation of the nuclear pore Nup107-160 subcomplex. Proc. Natl. Acad. Sci. U. S. A. *104*, 3811–3816.

Kim, S.J., Fernandez-Martinez, J., Nudelman, I., Shi, Y., Zhang, W., Raveh, B., Herricks, T., Slaughter, B.D., Hogan, J.A., Upla, P., et al. (2018). Integrative structure and functional anatomy of a nuclear pore complex. Nature *555*, 475–482.

Konishi, H.A., Asai, S., Watanabe, T.M., and Yoshimura, S.H. (2017). In vivo analysis of protein crowding within the nuclear pore complex in interphase and mitosis. Sci. Rep. *7*, 5709.

Laurell, E., Beck, K., Krupina, K., Theerthagiri, G., Bodenmiller, B., Horvath, P., Aebersold, R., Antonin, W., and Kutay, U. (2011). Phosphorylation of Nup98 by multiple kinases is crucial for NPC disassembly during mitotic entry. Cell *144*, 539–550.

Li, P., Banjade, S., Cheng, H.-C., Kim, S., Chen, B., Guo, L., Llaguno, M., Hollingsworth, J. V, King, D.S., Banani, S.F., et al. (2012). Phase transitions in the assembly of multivalent signalling proteins. Nature *483*, 336–340.

Linder, M.I., Köhler, M., Boersema, P., Weberruss, M., Wandke, C., Marino, J., Ashiono, C., Picotti, P., Antonin, W., and Kutay, U. (2017). Mitotic Disassembly of Nuclear Pore Complexes Involves CDK1- and PLK1-Mediated Phosphorylation of Key Interconnecting Nucleoporins. Dev. Cell *43*, 141–156.

Maximiliano A. D'Angelo and Martin W. Hetzer (2008). Structure, dynamics and function of nuclear pore complexes. Trends Cell Biol. *18*, 456–466.

Mohr, D., Frey, S., Fischer, T., Güttler, T., and Görlich, D. (2009). Characterisation of the passive permeability barrier of nuclear pore complexes. EMBO J. *28*, 2541–2553.

O'Neil, K.T., and DeGrado, W.F. (1990). A thermodynamic scale for the helix-forming tendencies of the commonly occurring amino acids. Science *250*, 646–651.

Otsuka, S., and Ellenberg, J. (2017). Mechanisms of nuclear pore complex assembly - two different ways of building one molecular machine. FEBS Lett. *592*, 475–488.

Otsuka, S., Szymborska, A., and Ellenberg, J. (2014). Imaging the assembly, structure, and function of the nuclear pore inside cells. Methods Cell Biol. *122*, 219–238.

Patel, S.S., Belmont, B.J., Sante, J.M., and Rexach, M.F. (2007). Natively unfolded nucleoporins

gate protein diffusion across the nuclear pore complex. Cell *129*, 83–96.

Piela, L., Némethy, G., and Scheraga, H.A. (1987). Proline-induced constraints in α-helices. Biopolymers *26*, 1587–1600.

Rabut, G., Doye, V., and Ellenberg, J. (2004). Mapping the dynamic organization of the nuclear pore complex inside single living cells. Nat. Cell Biol. *6*, 1114–1121.

Rauscher, S., Baud, S., Miao, M., Keeley, F.W., and Pomès, R. (2006). Proline and Glycine Control Protein Self-Organization into Elastomeric or Amyloid Fibrils. Structure *14*, 1667–1676.

Schmidt, H.B., and Görlich, D. (2015). Nup98 FG domains from diverse species spontaneously phase-separate into particles with nuclear pore-like permselectivity. Elife *4*, 1–30.

Solmaz, S., Chauhan, R., Blobel, G., and Melčák, I. (2011). Molecular architecture of the transport channel of the nuclear pore complex. Cell *147*, 592–602.

Woodruff, J.B., Wueseke, O., Viscardi, V., Mahamid, J., Ochoa, S.D., Bunkenborg, J., Widlund, P.O., Pozniakovsky, A., Zanin, E., Bahmanyar, S., et al. (2015). Centrosomes. Regulated assembly of a supramolecular centrosome scaffold in vitro. Science *348*, 808–812.

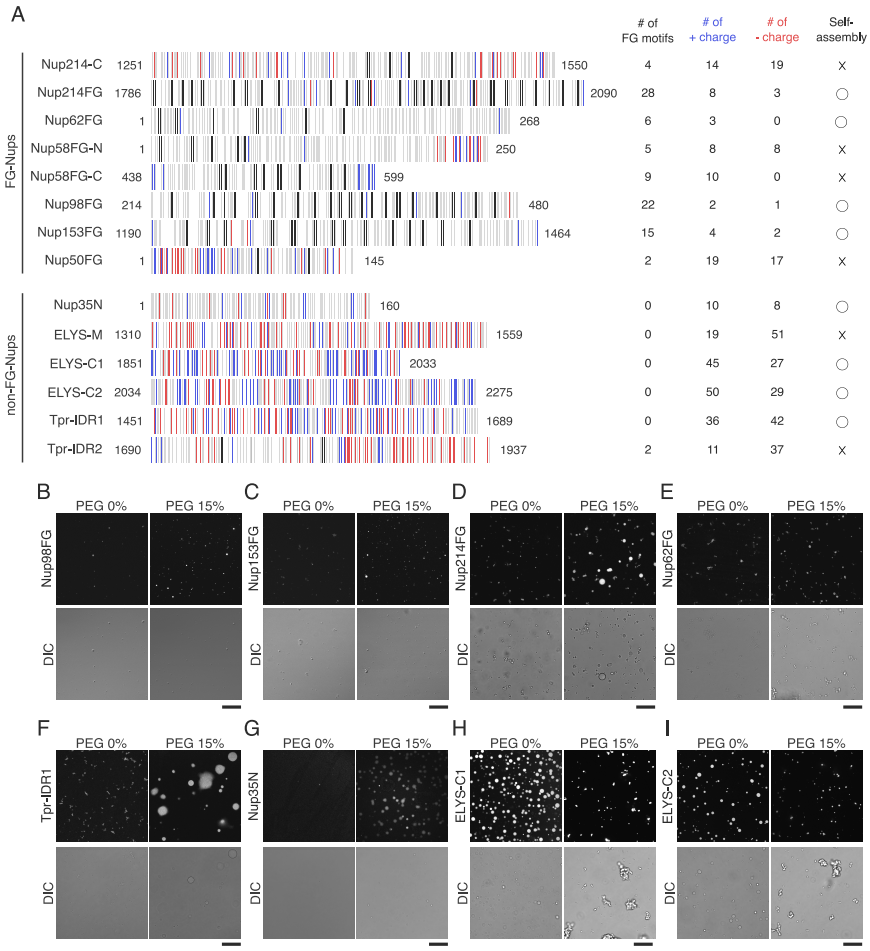

Konishi HA et al. Figure 1

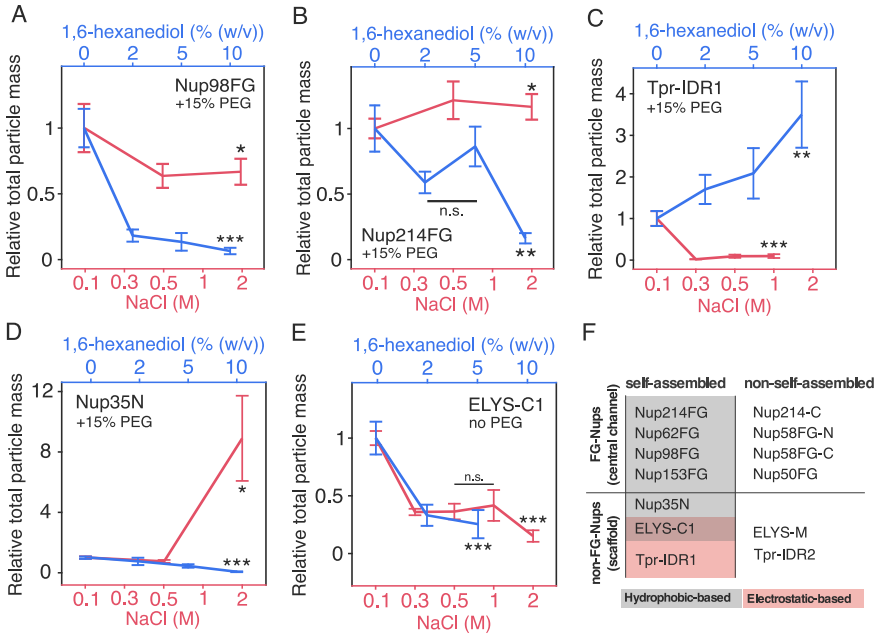

Konishi HA et al. Figure 2

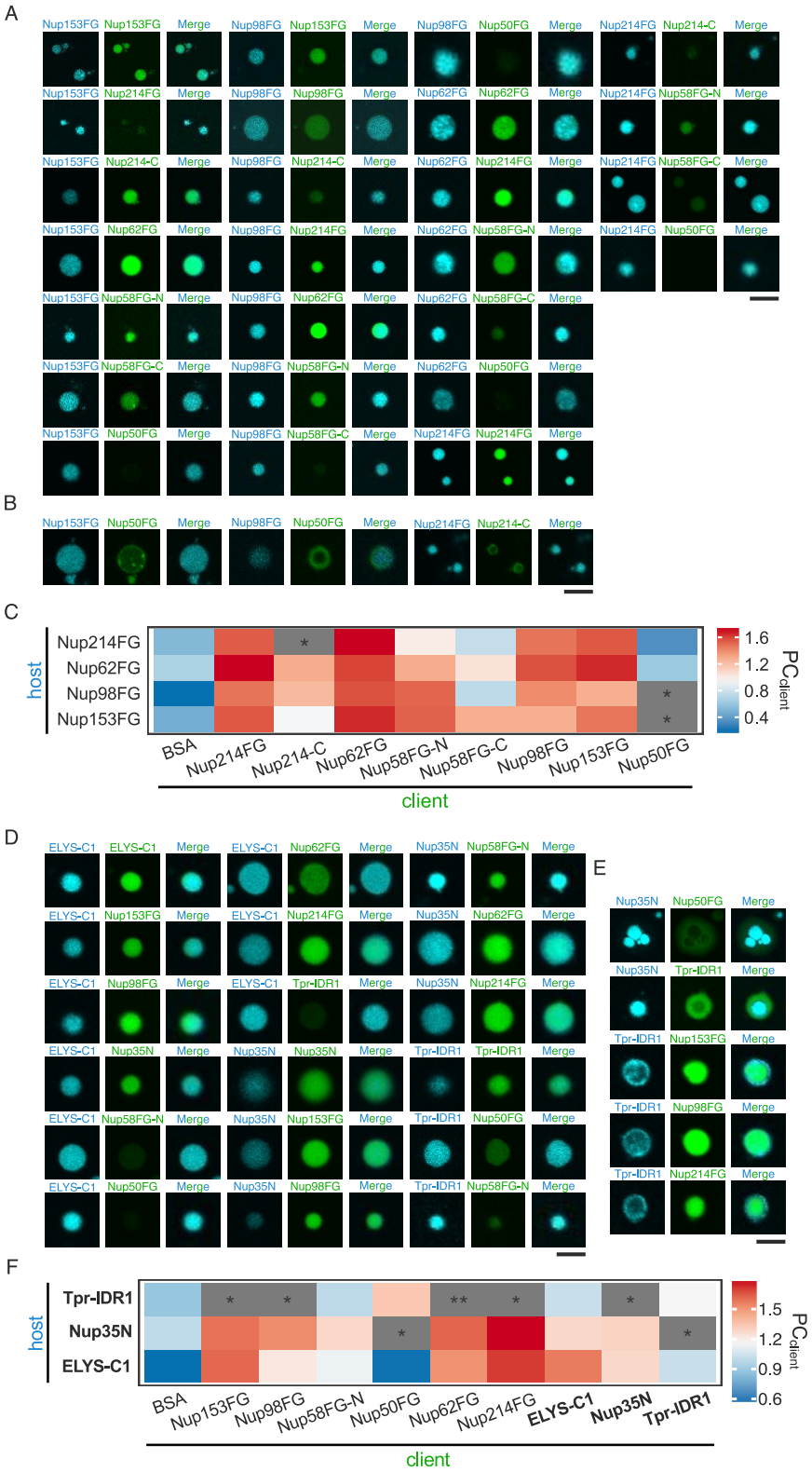

Konishi HA et al. Figure 3

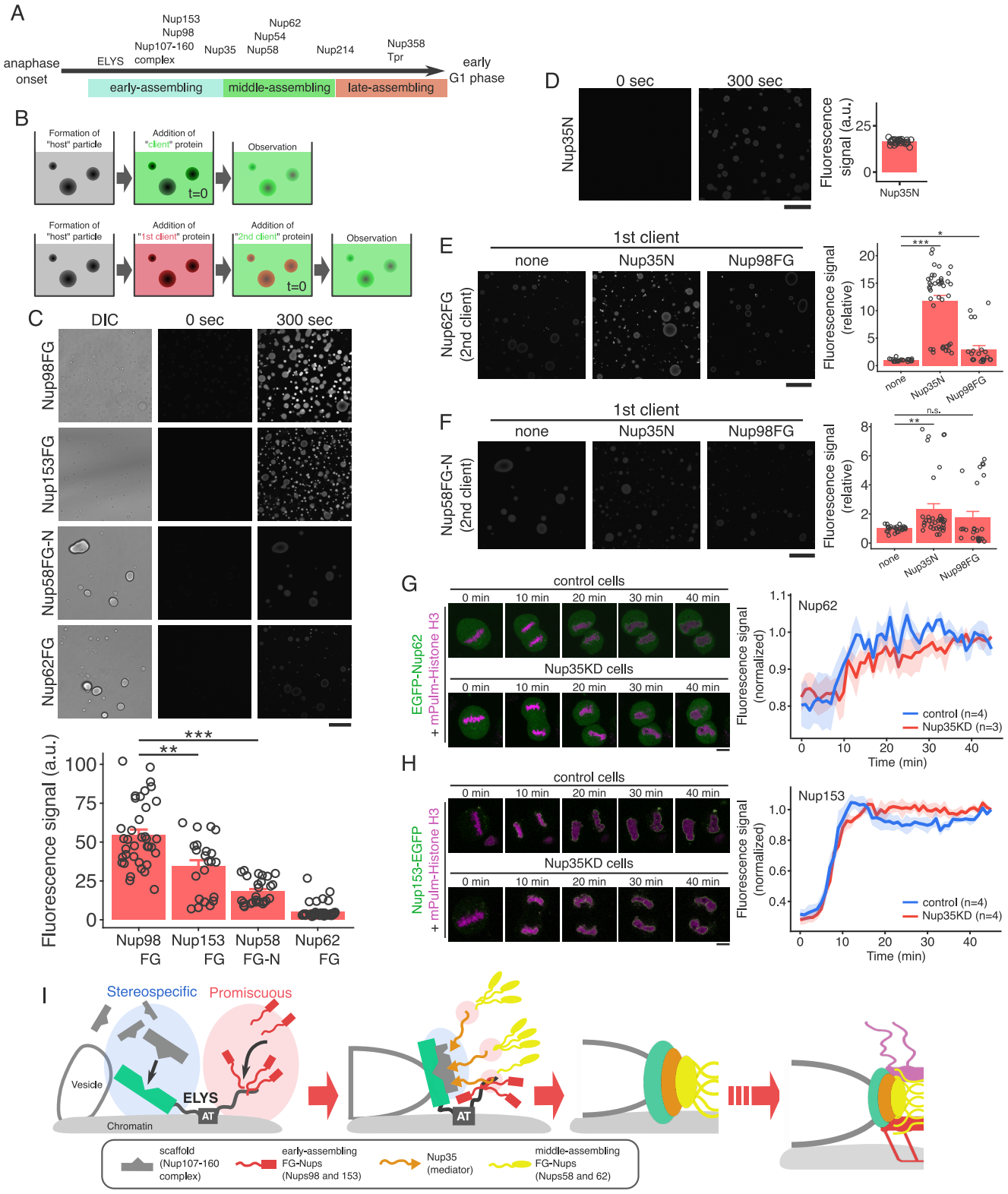

Konishi HA et al., Figure 4